From n- to p-Type Material: Effect of Metal Ion on Charge Transport in Metal−Organic Materials

Sungwon Yoon, A. Alec Talin, Vitalie Stavila, Austin M. Mroz, Thomas D. Bennett, Yuping He, David A. Keen, Christopher H. Hendon, Mark D. Allendorf,* and Monica C. So*

Cite This: https://doi.org/10.1021/acsami.1c09130

Read Online

ACCESS | �Ill Metrics & More | ☰ Article Recommendations | ☑ Supporting Information

ABSTRACT: An intriguing new class of two-dimensional (2D) materials based on metal−organic frameworks (MOFs) has recently been developed that displays electrical conductivity, a rarity among these nanoporous materials. The emergence of conducting MOFs raises questions about their fundamental electronic properties, but few studies exist in this regard. Here, we present an integrated theory and experimental investigation to probe the effects of metal substitution on the charge transport properties of M-HITP, where M = Ni or Pt and HITP = 2,3,6,7,10,11-hexaiminotriphenylene. The results show that the identity of the M-HITP majority charge carrier can be changed without intentional introduction of electronically active dopants. We observe that the selection of the metal ion substantially affects charge transport. Using the known structure, Ni-HITP, we synthesized a new amorphous material, a-Pt-HITP, which although amorphous is nevertheless found to be porous upon desolvation. Importantly, this new material exhibits p-type charge transport behavior, unlike Ni-HITP, which displays n-type charge transport. These results demonstrate that both p- and n-type materials can be achieved within the same MOF topology through appropriate choice of the metal ion.

KEYWORDS: metal−organic framework, metal−organic material, charge transport, electrical semiconductor, n-type, p-type, Seebeck, conductivity measurements
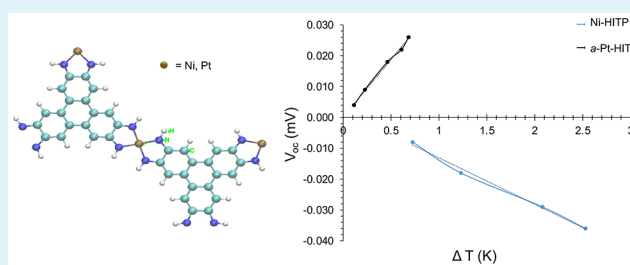
1. INTRODUCTION

Metal−organic frameworks (MOFs) are a rapidly expanding class of nanoporous materials composed of metal ions coordinated to multitopic organic linkers. However, the vast majority of MOFs are not electrically conducting. Their poor electronic charge transport properties have been recognized for some time as a major factor limiting their use in electronic device applications.[1−8] Conceptually, crystalline MOFs couple the long-range order and high thermal/chemical stability of inorganic conducting materials with the exceptional synthetic and chemical versatility of organic counterparts. In addition, their permanent nanoporosity provides a completely new design element, as well as the opportunity to introduce guest molecules as dopants to modulate their electrical properties. These characteristics make them distinct from conventional inorganic and organic porous materials, such as porous carbon and zeolites.[9] Recent work is gradually shedding light on the mechanisms of charge transport in MOFs and is identifying strategies for improving their electrical conductivity,[1,2] including structures that promote through-space conductivity ($\pi−\pi$ stacking),[10,11] through-bond conductivity,[12−15] redox-active structures,[4,7,16] and infiltration with noninnocent guest molecules.[5,8] These new synthetic concepts have only been realized in a few cases thus far.

A particularly promising recent development is the synthesis of metal−organic graphene (MOG) analogues, which are nanoporous layered structures with the same topology as graphene. The prototypical MOG, Ni₃ (2,3,6,7,10,11-hexaimi-notriphenylenesemiquinonate)₂ or Ni-HITP, for a time held the record as the MOF with the highest conductivity, with pressed pellets exhibiting a conductivity σ of 2 S cm^{-1} and an even higher 40 S cm^{-1} for thin films.[15] Since then, the thermoelectric properties of Ni-HITP have been reported,[17,18] as well as their use in chemiresistors,[19,20] supercapacitors,[21] and as an oxygen reduction catalyst.[22,23] This category of MOFs is expanding; other 2D layered MOF structures have been reported, such as M₃(HIB)₂ (M = Ni or Cu; HIB = hexaminobenzene)[24] and cobalt 2,3,6,7,10,11-triphenylenehex-athiolate.[25]

Unlike graphene and other inorganic 2D materials that offer very limited possibilities for chemical tunability of their

properties, these 2D semiconducting MOFs offer multiple synthetic routes for chemical modification. A potentially straightforward strategy is to substitute other metals. For example, in addition to the $M_3(HIB)_2$ structures referred to above, a $Cu_3(HITP)_2$ structure has been reported, which has a structure analogous to Ni-HITP, but is metallic.[19] However, the electrical conductivity of $Cu_3(HITP)_2$ is a factor of 10 lower than Ni-HITP. To explore the potential for chemically tuning the electronic structure, we used theory to suggest strategies that could improve the chemical tunability of Ni-HITP. Density functional theory (DFT) calculations performed by He and co-workers suggested that replacing the nickel metal ion with cations of larger ionic radii, such as platinum, would yield a higher Seebeck coefficient (S) and lower thermal conductivity κ, making these compounds potentially useful for thermoelectric applications.[26]

Later, Foster et al. proposed a second strategy, in which the layer spacing is increased by inserting a 4,4′-bipyridine (bpy) pillar ligand. Replacement of the Ni(II) ions with Cr(II) is also necessary to enable octahedral coordination.[27] In this case, the band gap of the optimized $Cr_3(HITP)_2(4,4'\text{-bpy})_3$ was predicted to be a much larger 1.43 eV.[28]

From the perspective of ease of synthesis, substituting Pt in the Ni-HITP structure is an appealing strategy, as this does not involve the synthesis of what would be essentially an entirely new MOF if the ligand were modified. Moreover, we expect the air stability of these materials to be significantly higher than structures involving Cr(II), which is prone to oxidation. Consequently, we pursued the more straightforward Pt substitution and herein describe the synthesis and characterization of the resulting in a new metal−organic material with spectroscopic and X-ray total scattering measurements. The synthesized Pt-HITP material intriguingly exhibits p-type electrical conductivity, in contrast with the n-type behavior of Ni-HITP,[21,28] while retaining significant porosity. Trends in the conductivity and S are consistent with our theoretical predictions.[29] These results indicate that, at a minimum, our metal substitution strategy succeeded in modulating the charge transport and properties without introduction of guest species as dopants.[30]

2. MATERIALS, METHODS, AND THEORETICAL CALCULATIONS

Materials. Starting materials were purchased from Sigma-Aldrich or VWR and were used without further purification. 2,3,6,7,10,11-hexaaminotriphenylene hexahydrochloride, HATP·6HCl, was prepared according to a procedure published elsewhere (Scheme S1).[15] THF was collected from an alumina column solvent purification system.

Syntheses. *Ni-HITP Powder.* A solution of HATP·6HCl(141.3 mg, 0.263 mmol, 1 equiv.) in DI water (20.0 mL) and a solution of $NiCl_2\cdot6H_2O$ (95.7 mg, 0.404 mmol, 1.5 equiv.) in DI water (30.0 mL) were combined in a 125 mL Erlenmeyer flask equipped with a septum, resulting in a brownish-yellow solution. The solution was heated to 65 °C, and NH_4OH (1.50 mL, 21.8 mmol, 83 equiv) was added. A black precipitate formed upon bubbling with air for 45 min, which was then bubbled with nitrogen for 2 h. (Note: The absence of air results in a brown solid within the transparent yellow solution. The formation mechanism of this material is uncertain, but we speculate that oxygen acts as a catalyst during synthesis.) The heterogeneous solution was centrifuged and the liquid layer was decanted. The resulting solid was washed with DI water (3 × 40 mL), ethanol (3 × 40 mL), and acetone (2 × 40 mL) with centrifugation and decanting after each wash. The final solid was dried under nitrogen for 15 h, resulting in a clumpy black powder (75.3 mg). Elemental analysis was performed by energy-dispersive X-ray spectroscopy (EDX). Calculated atomic ratio for Ni-HITP:C:N:Ni:O:Cl, 12:4:1:0:0. Found, 12:3.79:0.8:1.2:0.45.

a-Pt-HITP Powder. A solution of HATP·6HCl (141.7 mg, 0.263 mmol, 1 equiv.) in DI water (20.0 mL) and a solution of $(NH_4)_2PtCl_6$ (105.4 mg, 0.404 mmol, 1.5 equiv.) in DI water (30.0 mL) were combined in a 125 mL Erlenmeyer flask equipped with a septum, resulting in a colloidal burnt-red-brown solution. This solution was heated to 65 °C and NH_4OH (1.50 mL, 21.8 mmol, 83 equiv.) was injected, immediately turning the mixture a dark red-brown. The mixture was bubbled with air for 45 min, causing further darkening to an opaque black, and was then bubbled with nitrogen for 2 h. The mixture was washed and dried using the previous procedure, resulting in a clumpy black powder (94.8 mg). Calculated atomic ratios for Pt-HITP:C:N:Pt:O:Cl, 12:4:1:0:0. Found by EDX: 15.2:5.0:1.0:2.3:0.18. Found by elemental analysis, 13.2:4.4:1.0:1.7:0.2.

Characterization. ^1H NMR chemical shifts are reported in ppm and referenced to the residual solvent peak $Cl_2CDCDCl_2$ (δ = 5.93 ppm, ^1H), $CDCl_3$ (δ = 7.26 ppm, ^1H) and D_2O (δ = 4.79 ppm, ^1H) as an internal standard. NMR spectra are recorded on an Agilent NMR spectrometer operating at 499.69 MHz proton NMR frequency and the data analysis was performed using the *MestReNova* software package v. 11.0.4.

Powder X-ray diffraction (PXRD) experiments were carried out using a PANalytical Empyrean diffractometer equipped with a PIXcel3D detector operating in scanning line detector mode utilizing 255 channels. The diffractometer is outfitted with an Empyrean Cu LFF (long fine focus) HR DK386079 XRD tube operated at 45 kV and 40 mA, and Cu K-alpha radiation ($\lambda\alpha$ = 1.5418704 Å) was used for diffraction. Experiments were conducted in continuous scanning mode with the goniometer in the 2θ orientation. Incident beam optics included the Fixed Divergences slit with Antiscatter slit PreFIX module, with a 1/32° divergence slit and a 1/16° antiscatter slit, as well as a 10 mm fixed incident beam mask and a Soller slit (0.04 rad). Divergent beam optics included a P7.5 antiscatter slit, a Soller slit (0.04 rad), and a Ni Beta filter. The samples were typically dry and ground into a fine powder, applied to a low background sample holder and mounted to a bracket flat sample stage. In a typical experiment, data were collected via a continuous scan in the range of 3−60° (2θ) with a step size of 0.0131° and a scan time of 600 s per step.

Scanning electron microscopy (SEM) images were recorded using an FEI XL30s SEM equipped with a thermally assisted Schottky field-emission gun operated at an acceleration voltage of 10 kV and an effective working distance of 8 mm. For a higher image quality and to avoid charging effects, samples were coated with a 3 nm layer of Au. The substrates were then mounted onto the sample holder using copper tape.

X-ray total scattering data were collected at room temperature using a PANalytical Ag-source Empyrean lab diffractometer (λ = 0.561 Å). Data collection was carried out using loaded 1.0 mm diameter quartz capillaries and collection times of approximately 6 h. Background, multiple scattering, container scattering, Compton scattering, and absorption corrections were performed using the *GudrunX* program.[31,32] These data were subsequently processed using PDFGUI.

Elemental analyses (EA) for the elements C, H, N, and O were carried out using a Hekatech EuroEA Elementary Analysator. Metal contents (Pd and Pt) were determined photometrically on a Shimadzu UV-160 after acidic decomposition of the sample. For quantification of Cl, the sample was thermally decomposed at 1000 °C and collected in a sodium hydroxide/hydrazine sulfate solution. The chloride content was then determined by potentiometric titration of the solution versus $AgNO_3$ using a Metrohm 904 Titrando.

Raman spectra were obtained from 20 scans of each sample at λ = 532 nm using 50× objective and 100 mW/cm^2 laser power were collected on a Renishaw inVia Raman Microscope.

Nitrogen isotherms were collected at 77 K and carried out via the method of gas adsorption manometry using a ASAP 2020 automated surface area and pore size analyzer (Micromeritics, USA). The data were evaluated using the *QuadraWin* software V.5.02 (Quantachrome
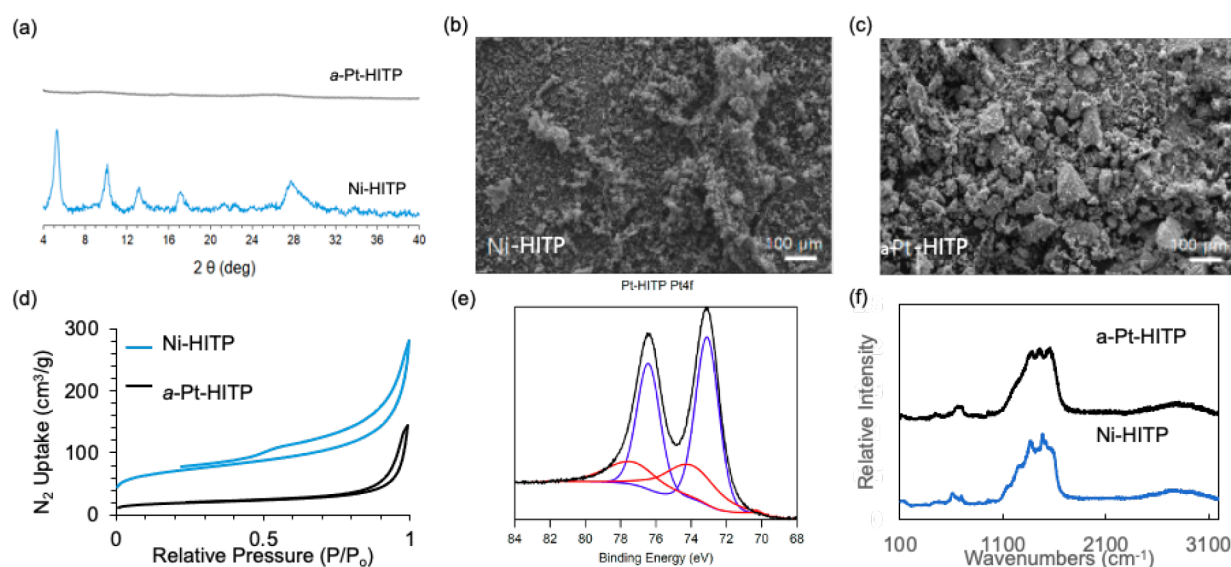
Figure 1. (a) PXRD, (b, c) SEM images, (d) N_2 adsorption−desorption isotherms, (e) XPS of Pt 4f peak for Pt-HITP, and (f) Raman spectra of Ni-HITP and *a*-Pt-HITP.

Instruments, USA). Prior to adsorption analysis all samples were outgassed for extended periods under dynamic turbomolecular pump vacuum and heating profiles described in the activation protocols. Outgassing was achieved using a MasterPrep 6 station degasser in vacuum mode with CN616 control software (Quantachrome Instruments, USA). Upon completion of the degas/heat profile, the samples were backfilled with dry N_2 (UHP). Data were analyzed with the Quantachrome QuadraWin software. Multipoint BET surface areas were calculated from 10 points spaced between $P/P° = 0.005$ and 0.075. Ambient temperature adsorption isotherms were collected from $P/P° = 0.01-1.00$. $P°$ was set to 760 mmHg.[1] The clearing of the pores, referenced from Wu et al., was done by soaking the powders in water at 100 °C (3×12 h) and then ethanol at 78 °C (3×12 h). Activation was completed under dynamic vacuum to 50 μmHg while ramping the temperature 2 °C/min, followed by holding at 60 °C until pressure calibrated. Once the low pressure was obtained, the temperature was increased by 2 °C/min and held at 100 °C for 6 h.[11]

X-ray photoelectron spectroscopy (XPS) measurements were taken on Omicron model DAR400 anode with a Physical Electronics model 10−360 electron energy analyzer detector and Al Kα anode (photon energy of 1486.6 eV). The base pressure of the measurement chamber was 1×10^{-10} Torr. The samples were cleanly transferred from an Ar glovebox to the XPS using custom-built vacuum suitcases. The binding energies were calibrated to the adventitious C 1s peak at 285.0 eV. Peak locations and widths were obtained by using Shirley backgrounds and fitting the collected data to mixed Gaussian-Lorentizan (70/30) lineshapes in the *CasaXPS* software.

Electrical conductivity. Electrical conductivity was measured in two-electrode configuration on pressed pellets using thin copper sheets for making electrical contacts. The pellets typically required 5 tons of force for pressing and consumed 30−70 mg of material, resulting in a thickness of the powder pellets ranging from 0.3 to 0.7 mm.

3. RESULTS

3.1. Synthesis and Characterization of *a*-Pt-HITP.
The amorphous Pt-HITP (*a*-Pt-HITP) compound was formed by the reported procedure[14] for Ni-HITP involving multiple soaks with water and EtOH at room temperature, followed by drying under a vacuum at 100 °C for 6 h. In the original synthetic method reported for Ni-HITP, it was shown that chlorine-free material can be obtained by extensive refluxing with water and

acetone.[15] However, it was subsequently reported that this also reduces the electrical conductivity.[17]

Unlike that of the Ni-HITP material, the PXRD of the *a*-Pt-HITP samples indicated that the powder is essentially amorphous (Figure 1a). SEM images show a granular morphology for both MOFs (Figure 1b, c), although particles are irregularly shaped. N_2 isotherms at 77 K (Figure 1d) reveal that *a*-Pt-HITP has a BET surface area of 67 m^2/g and Type IVa isotherms with Type H3 hysteresis loop. This is consistent with mesoporous materials in which capillary condensation occurs.[33] Isotherms of this type have been reported for other 2D MOFs similar to Ni-HITP.[25] However, these values, as well as the value of 250 m^2/g we obtained for Ni-HITP, are lower than previously reported for Ni-HITP (630 m^2/g).[17] This suggests that solvent molecules are partially filling the pores, consistent with the milder activation procedure we used above. Note that our attempts to synthesize the Pd-HITP analogue resulted in an amorphous material with incorrect stoichiometry compared to what is expected for $M_3(HITP)_2$ (Figures S2, S4, S6, S7; Tables S1 and S2). Consequently, we will not consider it further, although this material is interestingly both porous and electrically conducting (Figures S10 and S11).

To compare the composition of *a*-Pt-HITP to Ni-HITP, we collected elemental analyses and XPS data of the material. Table 1 indicates that *a*-Pt-HITP has a stoichiometry close to that of Ni-HITP $(Ni_3(C_{18}H_{12}N_6)_{1.8}Cl_{0.6}\cdot4(H_2O))$. If we normalize to three metal atoms, as in Ni-HITP, an atomic formulas for the *a*-Pt-HITP compound of $Pt_3(C_{18}H_{12}N_6)_{2.2}Cl_{1.7}\cdot5(H_2O)$ is obtained. The differences compared with the expected $M_3(HITP)_2$ stoichiometry is

Table 1. Atomic and Metal:Ligand Ratios Determined from Elemental Analysis

	C:M (HITP:M)	N:M (HITP:M)
theoretical[a]	12 (0.67)	4 (0.67)
Ni-HITP	12 (0.67)	3.79 (0.67)
Pt-HITP	13.2 (0.73)	4.4 (0.73)

[a]Based on $M_3(C_{18}H12N6)2$.

Table 2. Raman Bands of Ni-HITP and Pt-HITP from Both Experimental Measurements and Electronic Structure Calculations

experimental results	freq (cm^{-1})	rel. int.	electronic structure calculations	freq (cm^{-1})	rel. int.	assignments
crystalline Ni-HITP	600−800	0.10	modeling Ni-HITP	500−700	0.30	C−N and N−Ni bending
	1300−1500	0.62		1300−1600	0.30	C=C stretching
amorphous Pt-HITP	600−800	0.04	modeling Pt-HITP	500−700	0.40	C−N and N−Pt bending
	1300−1500	0.32		1300−1600	0.35	C=C stretching

due to excess chloride and water in the pores. This is consistent with elemental analyses data in Table S1, as well as the XPS data in Table S2 and Figures S3 and S5. XPS spectra (Figure 1e) of *a*-Pt-HITP powders show no evidence of Pt^{4+}, which would suggest octahedral coordination. In fact, high-resolution analysis of the Pt(4f) regions of the XPS spectra shows that the platinum metal exhibits a +2 oxidation state, consistent with that of the Ni-HITP material.

3.2. Raman Spectroscopy and Density of State Calculations. We observed Raman signals from three regions at 2500−3200 cm^{-1}, 1300−1500 cm^{-1}, and 600−800 cm^{-1} for the crystalline Ni-HITP and *a*-Pt-HITP. (Figure 1f) The broad peaks within the 2500−3200 cm^{-1} region observed in experiments for both materials resemble bands found in the spectrum of multilayer graphene[34] and do not appear in the calculated Raman spectra for monolayers, indicating that the synthesized materials likely have multilayered stacking of graphene-like sheets.[35] Furthermore, one can see that the *a*-Pt-HITP samples have almost identical peaks in the three regions as the crystalline Ni-HITP (Figure 1f). However, the relative intensities of those bands are different for the crystalline and the amorphous samples, which provides an opportunity to observe structural change due to what is likely the presence of hydrated chlorides. To assign the three regions to their corresponding vibrational modes, we performed electronic structure calculations (Figure S13) for M-HITP (M = Ni, Pt); these were also assigned by visual inspection (Table 2). We are interested in two regions: the bands at 600−800 cm^{-1} associated with the C−N and N−metal bonds and at 1300−1500 cm^{-1} associated with the C=C bonds. The ratio of band intensity at 600−800 cm^{-1} to that at 1300−1500 cm^{-1} decreased from 0.16 to 0.13 when comparing crystalline Ni-HITP to amorphous Pt-HITP. Slightly fewer N−Pt or C−N vibrations were present due to defects, likely originating from hydrated chlorides trapped between layers of *a*-Pt-HITP.

3.3. PDF Measurements. Given the amorphous PXRD data, the atomic structure of Pt-HITP was analyzed by the pair distribution function (PDF) method (Figure 2). The experimental PDF of Pt-HITP is broadly similar to the experimental Ni-HITP up to 4 Å, indicating that the coordination spheres and the linker molecule structure are similar. The PDF of Pt-HITP (Figure S8) shows peaks up to 6.5 Å, revealing the presence of chemical short-range order. The calculated $G(r)$ for Ni-HITP is also shown in Figure 2a, alongside the experimental $G(r)$. Peaks at 1.4 Å (1) and 1.9 Å (2) are consistent with C−C and Ni−O bonding, whereas the region at ca. 2.5 Å (3) is crowded with atom−atom correlations that do not correspond to bonds, including N−N, Ni−C and cross-ring C−C distances. The peak present at 3.1 Å (4) in the experimental $G(r)$ is correlated to hydrated chloride, an impurity in between the layers unrelated to the MOF structure. Key correlations include those at 4.1 Å (5) peak and at 4.9 Å (6), which are assigned to interlayer Ni−Ni and Ni−N distances (Figure 2b). The corresponding correlation (Pt−N) in the Pt-HITP sample appears lengthened
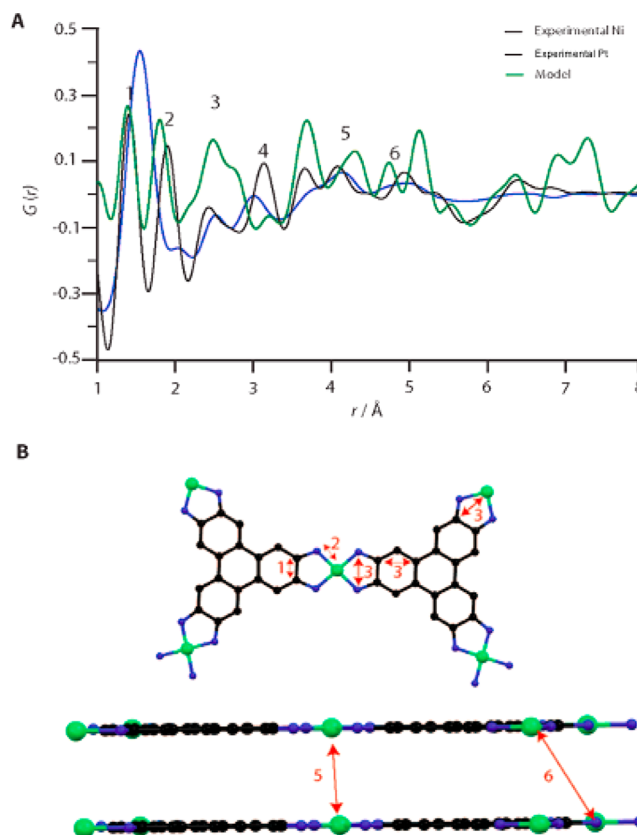

Figure 2. (a) Pair distribution function $G(r)$ for the experimental Ni-HITP (black), calculated Ni-HITP using 1/16th slipped model (green), and experimental Pt-HITP (blue). (b) Peak assignments using the structure for Ni-HITP. Ni, green; N, blue; C, black; H, omitted.

from 4.1 to 4.3 Å (Figure 2a). Compared with the HITP molecules in Ni-HITP, the Pt−N bonds in Pt-HITP became longer, corresponding to the insertion of a larger metal ion.

3.4. Charge Transport Properties. Because Pt-HITP has the same coordination environment as Ni-HITP based on the aforementioned results and likely also possesses a layered structure similar to Ni-HITP, it is reasonable to expect some level of electronic conductivity. As seen in Table 3, Pt-HITP is indeed electronically conducting with a conductivity about 67% higher than that of Ni-HITP. Although the measured conductivity values are lower than previously reported for the Ni-HITP,[17] the modest increase (~67%) with metal substitution is consistent with theory, which does not predict

Table 3. Conductivity Values and Seebeck Coefficients for Ni-HITP and *a*-Pt-HITP

compd	σ (S cm^{-1})	S (μV K)
Ni-HITP	0.195	−13.4
a-Pt-HITP	0.327	37.7

a drastic effect.[26] This is also consistent with the expectation that increasing the size of a metal cation size, and correspondingly its polarizability, increases the conductivity.

We also performed measurements of the Seebeck (S) to determine the majority charge carrier of Pt-HITP using an approach that was previously described in ref 7. Intriguingly, these measurements show that Pt-HITP is p-type, as indicated by its positive Seebeck coefficient. In contrast, our Ni-HITP pellets exhibited a negative room temperature S coefficient, as shown in Figure 3, indicating an n-type majority carrier material.[17] These results are consistent with both theory and previous reports.[26,28]
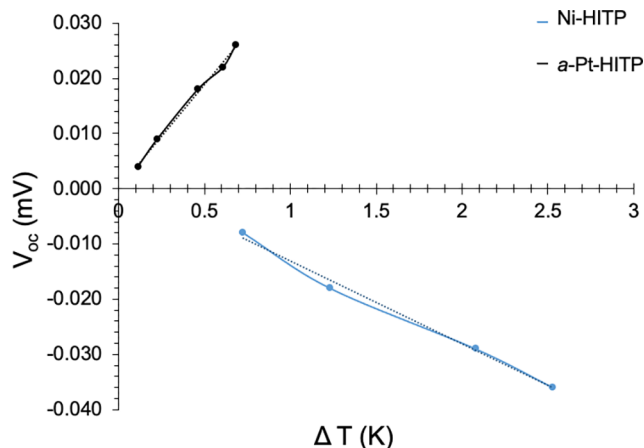

Figure 3. Thermovoltage characteristics of the nickel compound show n-type behavior (negative slope), whereas the platinum compound exhibits p-type behavior.

4. DISCUSSION

The presence of disorder in the Pt-HITP samples is not surprising, as even the most carefully synthesized MOFs contain a variety of defects.[36−41] Limited crystallinity is also common in cousins of MOFs—triazine-based covalent-organic frameworks (COFs).[42] The observation that our new a-Pt-HITP material exhibits both semiconducting behavior and porosity is consistent with previous DFT studies, which predicted that metal substitution in the Ni-HITP framework changes the electronic properties of these 2D frameworks from semiconducting to metallic.[43−47] Additional reasons for semiconducting behavior could be the amorphous nature of the Pt-HITP, which may lead to Anderson-type localization.[48]

The disorder in the M-HITP analogues likely stems from the presence of hydrated chlorides between these sheets, increasing the disorder of the materials. Counterions between platinum chain complexes have been shown to increase interchain distances to greater than 6.8 Å, introducing distortion between the chains.[49] Hydrated chloride ions between adjacent sheets of M-HITP may alter their structural conformation. In fact, when excess amounts of chloride are introduced into Ni-HITP, its unit cell expands by 4 Å, and the framework staggers by 1/16 fractional coordinates in the a and b directions[15] (Figure S9). As seen in Table S3, this resulted in some changes in the conductivity, but there is no clear trend. Because the layers are held together by weak forces, larger metals push these layers apart, enabling slippage and insertion of ions to be possible.

The most intriguing feature of the Pt-HITP is its p-type electronic conductivity, which contrasts with the n-type behavior of Ni-HITP. Several factors may contribute to the unique behavior of the M-HITP MOFs. First, based on previous computational results, the Pt-HITP unit cell should be larger than that of Ni-HITP because of the larger ionic radius of the metal ions.[26] Consequently, the indirect bandgap increases as the metal ion changes from Ni to Pt.[26] Second, although MOFs typically exhibit band gaps of several electronvolts, the predicted indirect band gap of the Pt analogues is small, ranging from 0.25 to 0.42 eV. Finally, whereas the computed conduction band dispersion is similar for both MOFs, the valence band dispersion increases by substituting Pt metal ions for the Ni, as computed by He and co-workers.[26] This suggests that the Pt-HITP should be a better p-type conductor than Ni-HITP, as is observed experimentally. Most significantly, however, these results demonstrate that metal substitution can be used to tailor the charge transport properties of 2D MOFs, in particular the identity of the majority charge carrier. This strategy has a considerable advantage over doping by inserting noninnocent guest molecules in the pores, as the forces binding guests to the pore walls may not be sufficient to prevent diffusion and loss of dopant.

5. CONCLUSIONS

To the best of our knowledge, this is the first demonstration that the majority carrier of a metal−organic material can be changed without conventional oxidative or reductive doping. Indeed, we accomplished this without using high reaction temperatures or inert conditions, suggesting that these materials could be compatible with other temperature-sensitive components of electronic devices. Importantly, our results confirm previous theoretical predictions, in which conductivity and power factors are predicted to increase with the atomic radius of the metal used for MOG formation. The various structural and spectroscopic data presented here are consistent with a local atomic arrangement surrounding the Pt ions that resembles that of Ni-HITP. Additional evidence supporting the formation of Pt-analogues of the Ni MOG are the similarity of the computed and measured PDF peak positions to predicted ones, at least in the low r region. Finally, the Pt MOG analogue exhibits particle morphology (as indicated by the SEM images) and Raman shifts that are very similar to Ni-HITP.

The results of this work have important implications for improving existing 2D MOGs for charge transport. Typically, increased electrical conductivity in a material is achieved through optimization of hierarchical structure or controlled chemical doping. In contrast, our measurements using pellets of Pt-HITP reveal S that metal substitution results in a change from n-type to p-type conductivity. This suggests the possibility that the electronic properties of MOGs can be tailored either by synthesizing bimetallic M′M′′-HITP complexes using non platinum-group metals or by tuning the majority carrier using different ratios of Ni/Pt within the MOG structure. Although principles for achieving high electrical conductivity in MOFs are now emerging, improvements in the Seebeck coefficient require fine-tuning of the band structure, an aspect of MOGs and MOFs in general that has received little attention. Finally, whereas a MOF crystal structure is obviously of considerable importance and has enabled MOFs to reach the level of chemical prominence that they enjoy today, this does not always represent the complete story.[50]

Nevertheless, the synthesis of porous Pt-HITP provides further evidence that amorphous structures are a subclass of MOFs that deserve consideration for their potential to create materials with unexpected but valuable properties.[51,52]

■ ASSOCIATED CONTENT

ⓈI Supporting Information

The Supporting Information is available free of charge at https://pubs.acs.org/doi/10.1021/acsami.1c09130.

> Synthesis of HATP·6HCl and associated ^{1}H NMR spectra, elemental analysis data, SEM, EDXS, EA, SEM, room-temperature conductivity measurements, experimental and simulated PXRD, PDF data and analyses parameters, and ab initio quantum mechanics calculations (PDF)

■ AUTHOR INFORMATION

Corresponding Authors

Monica C. So − *Department of Chemistry and Biochemistry, California State University Chico, Chico, California 95973, United States;* ⓘ orcid.org/0000-0002-9044-4806; Email: mso@csuchico.edu

Mark D. Allendorf − *Sandia National Laboratories, Livermore, California 94551, United States;* ⓘ orcid.org/0000-0001-5645-8246; Email: mdallen@sandia.gov

Authors

Sungwon Yoon − *Department of Chemistry and Biochemistry, California State University Chico, Chico, California 95973, United States; Department of Chemistry, University of Houston, Houston, Texas 77204, United States*

A. Alec Talin − *Sandia National Laboratories, Livermore, California 94551, United States;* ⓘ orcid.org/0000-0002-1102-680X

Vitalie Stavila − *Sandia National Laboratories, Livermore, California 94551, United States;* ⓘ orcid.org/0000-0003-0981-0432

Austin M. Mroz − *Department of Chemistry and Biochemistry, University of Oregon, Eugene, Oregon 97401, United States;* ⓘ orcid.org/0000-0003-4166-8093

Thomas D. Bennett − *Department of Materials Science and Metallurgy, University of Cambridge, Cambridge CB3 0FS, United Kingdom;* ⓘ orcid.org/0000-0003-3717-3119

Yuping He − *Department of Chemistry, University of Houston, Houston, Texas 77204, United States;* ⓘ orcid.org/0000-0003-0829-8086

David A. Keen − *ISIS Facility, Rutherford Appleton Laboratory, Didcot OX11 0QX, United Kingdom*

Christopher H. Hendon − *Department of Chemistry and Biochemistry, University of Oregon, Eugene, Oregon 97401, United States;* ⓘ orcid.org/0000-0002-7132-768X

Complete contact information is available at: https://pubs.acs.org/10.1021/acsami.1c09130

Author Contributions

The manuscript was written through contributions of all authors.

Notes

The authors declare no competing financial interest.

■ ACKNOWLEDGMENTS

■ REFERENCES

(1) Sun, L.; Campbell, M. G.; Dincǎ, M. Electrically conductive porous metal-organic frameworks. *Angew. Chem., Int. Ed.* **2016**, *55*, 3566−3579.

(2) Stassen, I.; Burtch, N.; Talin, A.; Falcaro, P.; Allendorf, M.; Ameloot, R. An updated roadmap for the integration of metal-organic frameworks with electronic devices and chemical sensors. *Chem. Soc. Rev.* **2017**, *46*, 3185−3241.

(3) Park, S. S.; Hontz, E. R.; Sun, L.; Hendon, C. H.; Walsh, A.; Van Voorhis, T.; Dincǎ, M. Cation-dependent intrinsic electrical conductivity in isostructural tetrathiafulvalene-based microporous metal-organic frameworks. *J. Am. Chem. Soc.* **2015**, *137*, 1774−1777.

(4) Sun, L.; Hendon, C. H.; Minier, M. A.; Walsh, A.; Dinca, M. Million-fold electrical conductivity enhancement in Fe$_2$(DEBDC) versus Mn$_2$(DEBDC)(E = S, O). *J. Am. Chem. Soc.* **2015**, *137*, 6164−6167.

(5) Talin, A. A.; Centrone, A.; Ford, A. C.; Foster, M. E.; Stavila, V.; Haney, P.; Kinney, R. A.; Szalai, V.; El Gabaly, F.; Yoon, H. P.; Léonard, F.; Allendorf, M. D. Tunable electrical conductivity in metal-organic framework thin-film devices. *Science* **2014**, *343*, 66−69.

(6) Erickson, K. J.; Léonard, F.; Stavila, V.; Foster, M. E.; Spataru, C. D.; Jones, R. E.; Foley, B. M.; Hopkins, P. E.; Allendorf, M. D.; Talin, A. A. Thin film thermoelectric metal-organic framework with high Seebeck coefficient and low thermal conductivity. *Adv. Mater.* **2015**, *27*, 3453−3459.

(7) Sun, L.; Hendon, C. H.; Park, S. S.; Tulchinsky, Y.; Wan, R.; Wang, F.; Walsh, A.; Dincǎ, M. Is Iron Unique in Promoting Electrical Conductivity in MOFs? *Chem. Sci.* **2017**, *8*, 4450−4457.

(8) Shiozawa, H.; Bayer, B. C.; Peterlik, H.; Meyer, J. C.; Lang, W.; Pichler, T. Doping of metal-organic frameworks towards resistive sensing. *Sci. Rep.* **2017**, *7*, 1−8.

(9) Talin, A. A.; Jones, R. E.; Hopkins, P. E. Metal-organic frameworks for thermoelectric energy-conversion applications. *MRS Bull.* **2016**, *41*, 877−882.

(10) Takaishi, S.; Hosoda, M.; Kajiwara, T.; Miyasaka, H.; Yamashita, M.; Nakanishi, Y.; Kitagawa, Y.; Yamaguchi, K.; Kobayashi, A.; Kitagawa, H. *Inorg. Chem.* **2009**, *48*, 9048−9050.

(11) Kobayashi, Y.; Jacobs, B.; Allendorf, M. D.; Long, J. R. *Chem. Mater.* **2010**, *22*, 4120−4122.

(12) Sun, L.; Miyakai, T.; Seki, S.; Dincă, M. *J. Am. Chem. Soc.* **2013**, *135*, 8185−8188.

(13) Zhang, Q.; Li, B.; Chen, L. *Inorg. Chem.* **2013**, *52*, 9356−9362.

(14) Wu, G.; Huang, J.; Zang, Y.; He, J.; Xu, G. Porous field-effect transistors based on a semiconductive metal-organic framework. *J. Am. Chem. Soc.* **2017**, *139*, 1360−1363.

(15) Sheberla, D.; Sun, L.; Blood-Forsythe, M. A.; Er, S.; Wade, C. R.; Brozek, C. K.; Aspuru-Guzik, A.; Dinca, M. High Electrical Conductivity in $Ni_3(2,3,6,7,10,11$-hexaiminotriphenylene$)_2$, a Semiconducting Metal-Organic Graphene Analogue. *J. Am. Chem. Soc.* **2014**, *136*, 8859−8862.

(16) Xie, L. S.; Sun, L.; Wan, R.; Park, S. S.; DeGayner, J. A.; Hendon, C. H.; Dinca, M. Tunable Mixed-Valence Doping towards Record Electrical Conductivity in a Three-Dimensional Metal-Organic Framework. *J. Am. Chem. Soc.* **2018**, *140*, 7411−7414.

(17) Sun, L.; Liao, B.; Sheberla, D.; Kraemer, D.; Zhou, J.; Stach, E. A.; Zakharov, D.; Stavila, V.; Talin, A. A.; Ge, Y.; Allendorf, M. D.; Chen, G.; Léonard, F.; Dincă, M. A Microporous and Naturally Nanostructured Thermoelectric Metal-Organic Framework with Ultralow Thermal Conductivity. *Joule* **2017**, *1*, 168−177.

(18) Erickson, K. J.; Léonard, F.; Stavila, V.; Foster, M. E.; Spataru, C. D.; Jones, R. E.; Foley, B. M.; Hopkins, P. E.; Allendorf, M. D.; Talin, A. A. Thin film thermoelectric metal-organic framework with high Seebeck coefficient and low thermal conductivity. *Adv. Mater.* **2015**, *27*, 3453−3459.

(19) Campbell, M. G.; Sheberla, D.; Liu, S. F.; Swager, T. M.; Dincă, M. Cu_3(hexaiminotriphenylene)$_2$: an electrically conductive 2D metal-organic framework for chemiresistive sensing. *Angew. Chem., Int. Ed.* **2015**, *54* (14), 4349−4352.

(20) Campbell, M. G.; Liu, S. F.; Swager, T. M.; Dincă, M. Chemiresistive sensor arrays from conductive 2D metal-organic frameworks. *J. Am. Chem. Soc.* **2015**, *137* (43), 13780−13783.

(21) Sheberla, D.; Bachman, J. C.; Elias, J. S.; Sun, C. J.; Shao-Horn, Y.; Dincă, M. Conductive MOF electrodes for stable supercapacitors with high areal capacitance. *Nat. Mater.* **2017**, *16* (2), 220−224.

(22) Miner, E. M.; Fukushima, T.; Sheberla, D.; Sun, L.; Surendranath, Y.; Dincă, M. Electrochemical oxygen reduction catalysed by Ni_3(hexaiminotriphenylene)$_2$. *Nat. Commun.* **2016**, *7*, 1−7.

(23) Miner, E. M.; Gul, S.; Ricke, N. D.; Pastor, E.; Yano, J.; Yachandra, V. K.; Van Voorhis, T.; Dincă, M. Mechanistic evidence for ligand-centered electrocatalytic oxygen reduction with the conductive MOF Ni_3(hexaiminotriphenylene)$_2$. *ACS Catal.* **2017**, *7* (11), 7726−7731.

(24) Dou, J. H.; Sun, L.; Ge, Y.; Li, W.; Hendon, C. H.; Li, J.; Gul, S.; Yano, J.; Stach, E. A.; Dincă, M. Signature of metallic behavior in the metal-organic frameworks M_3(hexaiminobenzene)$_2$ (M= Ni, Cu). *J. Am. Chem. Soc.* **2017**, *139* (39), 13608−13611.

(25) Clough, A. J.; Skelton, J. M.; Downes, C. A.; De La Rosa, A. A.; Yoo, J. W.; Walsh, A.; Melot, B. C.; Marinescu, S. C. Metallic conductivity in a two-dimensional cobalt dithiolene metal-organic framework. *J. Am. Chem. Soc.* **2017**, *139* (31), 10863−10867.

(26) He, Y.; Spataru, C. D.; Léonard, F.; Jones, R. E.; Foster, M. E.; Allendorf, M. D.; Talin, A. A. Two-Dimensional Metal-Organic Frameworks with High Thermoelectric Efficiency Through Metal Ion Selection. *Phys. Chem. Chem. Phys.* **2017**, *19*, 19461−19467.

(27) Le, K. N.; Mancuso, J. L.; Hendon, C. H. Electronic Challenges of Retrofitting 2D Electrically Conductive MOFs to Form 3D Conductive Lattices. *ACS Appl. Electron. Mater.* **2021**, *3*, 2017−2023.

(28) Foster, M. E.; Sohlberg, K.; Spataru, C. D.; Allendorf, M. D. Proposed modification of the graphene analogue Ni-HITP to yield a semiconducting material. *J. Phys. Chem. C* **2016**, *120* (27), 15001−15008.

(29) He, Y.; Talin, A. A.; Allendorf, M. D. Thermoelectric Properties of 2D $Ni_3(HITP)_2$ and 3D $Cu_3(BTC)_2$ MOFs: First-Principles Studies. *ECS J. Solid State Sci. Technol.* **2017**, *6* (12), N236−N242.

(30) Syzgantseva, M. A.; Ireland, C. P.; Ebrahim, F. M.; Smit, B.; Syzgantseva, O. A. Metal Substitution as the Method of Modifying Electronic Structure of Metal-Organic Frameworks. *J. Am. Chem. Soc.* **2019**, *141* (15), 6271−6278.

(31) Soper, A. K. *Technincal Report. RAL-TR-2011−013: GudrunN and GudrunX: Programs for Correcting Raw Neutron and X-ray Diffraction Data to Differential Scattering Cross Section*; Science & Technology Facility Council: Swindon, U.K., 2011.

(32) Soper, A. K.; Barney, E. R. Extracting the pair distribution function from white-beam X-ray total scattering data. *J. Appl. Crystallogr.* **2011**, *44*, 714−726.

(33) Thommes, M.; Kaneko, K.; Neimark, A. V.; Olivier, J. P.; Rodriguez-Reinoso, F.; Rouquerol, J.; Sing, K. S. Physisorption of gases, with special reference to the evaluation of surface area and pore size distribution (IUPAC Technical Report). *Pure Appl. Chem.* **2015**, *87* (9−10), 1051−1069.

(34) Graf, D.; Molitor, F.; Ensslin, K.; Stampfer, C.; Jungen, A.; Hierold, C.; Wirtz, L. Spatially resolved Raman spectroscopy of single- and few-layer graphene. *Nano Lett.* **2007**, *7* (2), 238−242.

(35) Gupta, A.; Chen, G.; Joshi, P.; Tadigadapa, S.; Eklund, P. C. Raman scattering from high-frequency phonons in supported n-graphene layer films. *Nano Lett.* **2006**, *6* (12), 2667−2673.

(36) Cliffe, M. J.; Wan, W.; Zou, X.; Chater, P. A.; Kleppe, A. K.; Tucker, M. G.; Wilhelm, H.; Funnell, N. P.; Coudert, F. X.; Goodwin, A. L. Correlated defect nanoregions in a metal-organic framework. *Nat. Commun.* **2014**, *5* (1), 1−8.

(37) Øien, S.; Wragg, D.; Reinsch, H.; Svelle, S.; Bordiga, S.; Lamberti, C.; Lillerud, K. P. Detailed structure analysis of atomic positions and defects in zirconium metal-organic frameworks. *Cryst. Growth Des.* **2014**, *14* (11), 5370−5372.

(38) Bennett, T. D.; Cheetham, A. K.; Fuchs, A. H.; Coudert, F. X. Interplay between defects, disorder and flexibility in MOFs. *Nat. Chem.* **2017**, *9* (1), 11−16.

(39) Fang, Z.; Bueken, B.; De Vos, D. E.; Fischer, R. A. Defect-engineered metal-organic frameworks. *Angew. Chem., Int. Ed.* **2015**, *54* (25), 7234−7254.

(40) Sholl, D. S.; Lively, R. P. Defects in metal-organic frameworks: challenge or opportunity? *J. Phys. Chem. Lett.* **2015**, *6* (17), 3437−3444.

(41) Dissegna, S.; Epp, K.; Heinz, W. R.; Kieslich, G.; Fischer, R. A. Defective metal-organic frameworks. *Adv. Mater.* **2018**, *30* (37), 1704501.

(42) Hug, S.; Stegbauer, L.; Oh, H.; Hirscher, M.; Lotsch, B. V. Nitrogen-rich covalent triazine frameworks as high-performance platforms for selective carbon capture and storage. *Chem. Mater.* **2015**, *27* (23), 8001−8010.

(43) Foster, M. E.; Sohlberg, K.; Spataru, C. D.; Allendorf, M. D. Proposed Modification of the Graphene Analogue Ni3(HITP)2 To Yield a Semiconducting Material. *J. Phys. Chem. C* **2016**, *120*, 15001−15008.

(44) Shojaei, F.; Hahn, J. R.; Kang, H. S. Mechanical and electronic properties of π-conjugated metal bis (dithiolene) complex sheets. *Chem. Mater.* **2014**, *26*, 2967−2974.

(45) Chen, S.; Dai, J.; Zeng, X. C. Metal−organic Kagome lattices M3(2,3,6,7,10,11-hexaiminotriphenylene)2 (M = Ni and Cu): from semiconducting to metallic by metal substitution. *Phys. Chem. Chem. Phys.* **2015**, *17*, 5954.

(46) Chakravarty, C.; Mandal, B.; Sarkar, P. Multifunctionalities of an Azine-Linked Covalent Organic Framework: From Nanoelectronics to Nitroexplosive Detection and Conductance Switching. *J. Phys. Chem. C* **2018**, *122*, 3245−3255.

(47) Sun, L.; Hendon, C. H.; Park, S. S.; Tulchinsky, Y.; Wan, R.; Wang, F.; Walsh, A.; Dinca, M. Is iron unique in promoting electrical conductivity in MOFs? *Chem. Sci.* **2017**, *8*, 4450−4457.

(48) Prestigiacomo, J. C.; Nath, A.; Osofsky, M. S.; Hernández, S. C.; Wheeler, V. D.; Walton, S. G.; Gaskill, D. K. Determining the nature of the gap in semiconducting graphene. *Sci. Rep.* **2017**, *7*, 1−5.

(49) Otake, K. I.; Otsubo, K.; Sugimoto, K.; Fujiwara, A.; Kitagawa, H. Neutral-Type One-Dimensional Mixed-Valence Halogen-Bridged Platinum Chain Complexes with Large Charge-Transfer Band Gaps. *Inorg. Chem.* **2016**, *55* (5), 2620−2626.

(50) Allendorf, M. D.; Stavila, V.; Witman, M.; Brozek, C. K.; Hendon, C. H. What Lies beneath a Metal-Organic Framework Crystal Structure? New Design Principles from Unexpected Behaviors. *J. Am. Chem. Soc.* **2021**, *143* (18), 6705−6723.

(51) Bennett, T. D.; Horike, S. Liquid, glass and amorphous solid states of coordination polymers and metal-organic frameworks. *Nature Rev. Mater.* **2018**, *3* (11), 431−440.

(52) Cheetham, A. K.; Bennett, T. D.; Coudert, F. X.; Goodwin, A. L. Defects and disorder in metal organic frameworks. *Dalton Trans* **2016**, *45* (10), 4113−4126.